Prussian Blue Analogue-Derived ZnO/ZnFe$_2$O$_4$ Core-Shell Nanospheres as High-Performance Anodes for Lithium-Ion and Potassium-Ion Batteries

Qinglin Wang,[a] Libin Kang,[a] Zheng Xing,*[a] Chuanhao Nie,[a] Haiping Hong,[b] Xichen Zhou,[c] Qinbai Yun,[c] Zhicheng Ju,[a] and Bo Chen*[c]

Herein, core-shell nanostructured ZnO/derived from self-sacrifice template method with Prussian blue analogue (i.e., Zn$_3$[Fe(CN)$_6$]$_2$) as precursor has been successfully synthesized by controlling the calcination temperatures and heating rates. The formation mechanism of core-shell nanostructures has been explored through the morphology transformation under different synthetic conditions. Impressively, ZnO/ZnFe$_2$O$_4$ hybrid material with core-double shell nanostructure shows good cycling performance as anodes of lithium-ion batteries (1137 mAh g^{-1} at 1 A g^{-1} after 80 cycles) and potassium-ion batteries (217 mAh g^{-1} at 0.1 A g^{-1} after 400 cycles). The excellent performances can be attributed to the unique core-double shell nanostructure as well as synergistic effects of ZnO and ZnFe$_2$O$_4$. The results indicate that the strategy of designing nanostructures could successfully improve the electrochemical performances of ZnO/ZnFe$_2$O$_4$ and effectively expand the commercial application of transition metal oxides.

Introduction

In the last two decades, lithium-ion batteries (LIBs) have been extensively studied and used in several fields, including clean energy vehicles and home electronics, because of their good cycling stability, low price, and high energy density.[1–3] However, the low theoretical specific capacity of commercial graphite-based anodes (372 mAh g^{-1}) has restricted the further development of LIBs.[4,5] In addition to LIBs, potassium-ion batteries (PIBs) also have attracted extensive attention due to their low cost and high natural abundance. Although the working principle of PIBs is similar to that of LIBs, the application of traditional lithium-storage anodes in PIBs is limited due to the large ion radius of potassium.[6,7] It is imminent to develop safe and reliable anodes with high capacity for the further development of LIBs and PIBs as the next-generation energy-storage devices.[8–13]

Compared with commercial graphite-based anodes, transition metal oxides (TMOs) have been a research hotspot on account of their outstanding theoretical specific capacity (800–1200 mAh g^{-1}) and good environmental compatibility.[14] The lithium-storage mechanisms of TMOs are mainly divided into three types: insertion/extraction type, alloying/dealloying type, and conversion reaction type.[15] The lithium-storage mechanism of insertion/extraction type of TMOs is that lithium ions diffuse into the lattice of TMOs without redox reactions, only changing the structure of TMOs, so they have excellent cycling stability but relatively low capacity. The alloying/dealloying and conversion reaction types of TMOs, which have higher theoretical specific capacity than the insertion/extraction type, are based on the redox reactions. However, because of the lithium-storage mechanism of redox reactions, the alloying/dealloying and conversion reaction types of TMOs suffer from severe volume expansion and poor cycle stability during the charging/discharging process.[15–17]

As a typical binary TMO, ZnFe$_2$O$_4$ has an outstanding theoretical specific capacity (1072 mAh g^{-1}),[18] which could be ascribed to synergistic effects of the alloying/dealloying and conversion reaction mechanisms. ZnO is also a TMO with similar lithium-storage mechanisms. Because of the high theoretical specific capacities and the special lithium-storage mechanisms, ZnO and ZnFe$_2$O$_4$ have been intensively investigated as anodes for LIBs.[19–22] During the discharging process, lithium ions are intercalated into ZnFe$_2$O$_4$ to form Li$_x$ZnFe$_2$O$_4$ at first. After that, Li$_x$ZnFe$_2$O$_4$ is then reduced by the intercalation of lithium ions to form metallic Zn, Fe, and Li$_2$O. Finally, lithium ions react with metallic Zn and form LiZn alloy. Because of the formation of LiZn alloy, ZnFe$_2$O$_4$ has a higher capacity than other TMOs.[23–27] In the charging process, metallic Fe and Zn are oxidized by Li$_2$O separately to form Fe$_2$O$_3$ and ZnO.[28] Consequently, ZnFe$_2$O$_4$ has a lower working potential of about

[a] Q. Wang, L. Kang, Dr. Z. Xing, Dr. C. Nie, Prof. Z. Ju
School of Materials Science and Physics
China University of Mining and Technology
221116 Xuzhou, P. R. China
E-mail: xzh086@cumt.edu.cn
[b] Dr. H. Hong
South Dakota School of Mines and Technology
Department of Electrical Engineering
57701 Rapid City, SD, USA
[c] X. Zhou, Dr. Q. Yun, Dr. B. Chen
Department of Chemistry
City University of Hong Kong
Hong Kong, P. R. China
E-mail: bchen005@e.ntu.edu.sg

Batteries & Supercaps

Research Article
doi.org/10.1002/batt.202200411

Chemistry
Europe

European Chemical
Societies Publishing

1.5 V but higher specific capacity of 1072 mAh g^{-1} when compared to other TMOs. Despite these advantages, ZnFe$_2$O$_4$, as one of the most promising anodes, has suffered from the problems of rapid attenuation of specific capacity and poor rate performance due to severe volume expansion and nanostructure collapse. Moreover, when ZnFe$_2$O$_4$ is used as anode materials for PIBs, the larger radius of potassium-ion compared with that of lithium-ion will further lead to volume expansion and nanostructure collapse. Solving these problems is the first prerequisite for promoting ZnFe$_2$O$_4$ as commercial material.

Controlled synthesis of electrode materials with rationally designed nanostructures is an effective way to alleviate nanostructure collapse and volume expansion.[29,30] Rationally designed nanostructures can relieve the strain in the process of insertion/extraction of lithium ions and optimize diffusion paths of lithium ions. To date, researchers have designed various nanostructures (e.g., core-shell,[31] hollow octahedra,[32] and porous structures[28]) through different methods. The core-shell nanostructure considerably enhances the specific surface area of ZnFe$_2$O$_4$ and generates abundant electrochemical active sites when compared to other nanostructures. The cavity which between the core and shell can reduce the volume expansion in the charging/discharging process remarkably, which is helpful for improving the cycling stability.[33–36] In addition, the core-shell nanostructure can enrich the contact area with electrolytes as well as accelerate the diffusion rate of Li ions. Given these advantages, more and more researchers have begun to focus on designing core-shell nanostructures using different methods. For example, Yuan et al. used Zn$_3$[Fe(CN)$_6$]$_2$ as the self-sacrificing template to prepare core-shell mesoporous ZnO/ZnFe$_2$O$_4$@C, which remained a good discharge capacity of 893 mAh g^{-1} at 500 mA g^{-1} after 60 cycles.[31] Sun et al. explored polypyrrole-coated ZnFe$_2$O$_4$ double-shell hollow microspheres by the spray-drying method, with a discharge capacity of 698 mAh g^{-1} at 400 mA g^{-1} after 100 cycles.[35] Hou et al. successfully fabricated yolk-shell hollow ZnFe$_2$O$_4$/C by the bottom-up template-free approach, which still maintained a discharge capacity of 940 mAh g^{-1} at 500 mA g^{-1} after 500 cycles.[34] The above reports showed that different core-shell nanostructures could improve the electrochemical performance of ZnO/ZnFe$_2$O$_4$. However, the formation and change of the core-shell structure during the calcination process have not been studied in detail. In addition, there are relatively few reports on the potassium-storage properties of core-shell ZnO/ZnFe$_2$O$_4$.[37–39]

Herein, we report the preparation of ZnO/ZnFe$_2$O$_4$ core-shell nanospheres by the self-sacrificing template method. This simple method involves Zn$_3$[Fe(CN)$_6$]$_2$ as the precursor and modulates the core-shell nanostructure of the samples by changing the calcination temperatures as well as heating rates. The formation mechanism of core-shell nanostructures has been discussed through the changes in morphology and nanostructures at different synthetic conditions. Finally, according to the differences in the electrochemical properties of ZnO/ZnFe$_2$O$_4$ with different nanostructures, the relationship between nanostructures and electrochemical performances has been studied, which provides a reference for the further

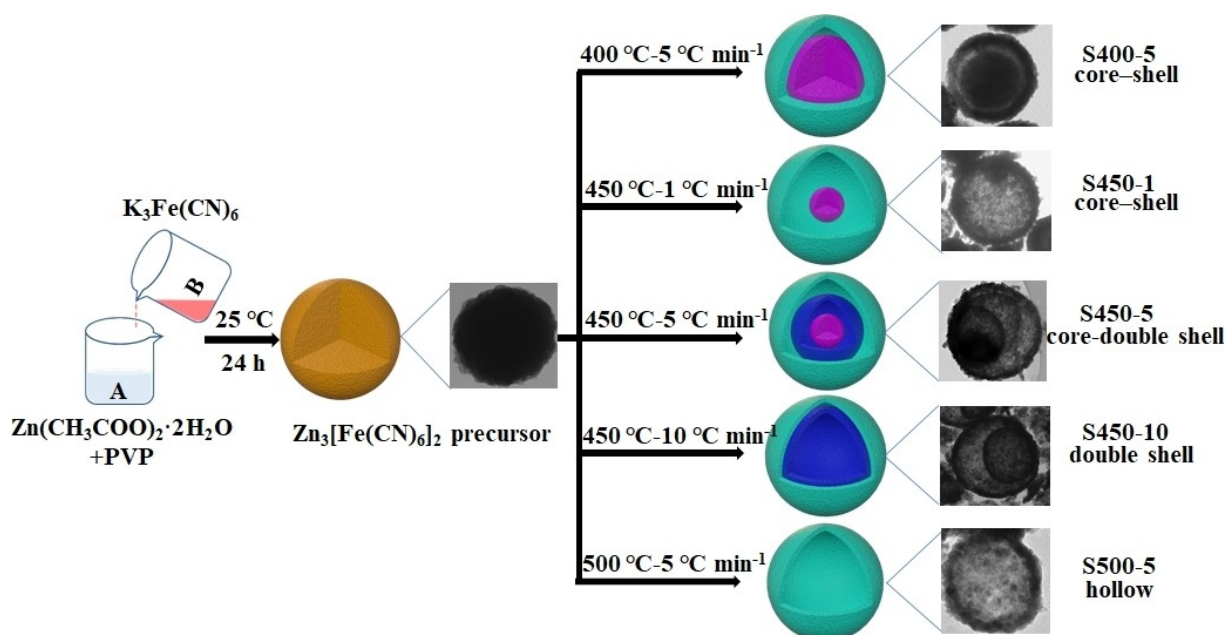development of TMOs as commercial anode materials for LIBs and PIBs.

Results and Discussions

Formation mechanism of core-shell nanostructures

Based on the self-sacrificial template method, core-shell nanostructured ZnO/ZnFe$_2$O$_4$ samples were successfully synthesized by calcining the Zn$_3$[Fe(CN)$_6$]$_2$ at various calcination temperatures and heating rates, as shown in Scheme 1. The formation mechanism of core-shell nanostructures could be attributed to the Kirkendall effect, which is caused by different diffusion rates in the diffusion couple.[40,41] During the calcination of the precursor, the diffusion rates of oxygen on the surface and interior parts of ZnO/ZnFe$_2$O$_4$ nanospheres are inconsistent, resulting in the formation of core-shell nanostructures.[31] More specifically, due to the high oxygen content, the outer surface of Zn$_3$[Fe(CN)$_6$]$_2$ nanospheres firstly forms a relatively rigid ZnO/ZnFe$_2$O$_4$ shell, which can provide adhesion forces. Subsequently, the decomposition of cyano groups inside the nanospheres can generate shrinkage forces. During the calcining process, the synergistic effect of shrinkage and adhesion forces transforms the nanostructures from solid spheres to core-shell nanostructures.[42,43] It should be noted that with the increasing of temperature, the adhesion force is much larger than the shrinkage force. This also explains the formation of hollow nanostructures when calcined at 500 °C.[29] In addition, numerous mesopores are presented in the core-shell nanoparticles due to the abundant gas generated during the decomposition of the cyano group.[28] The unique core-shell nanostructure not only improves the surface area for interaction with the electrolyte, but also provides more electrochemical active sites. In addition, it can offer buffer space to alleviate the volume expansion problem.[18,44]

Morphology and structure

The reaction temperature is generally known to be a crucial parameter in the self-sacrificial template method of forming ZnO/ZnFe$_2$O$_4$. Figure 1a displays the TGA profile of the decomposition process of Zn$_3$[Fe(CN)$_6$]$_2$, which could be divided into three parts: Below 240 °C, about 25% weight loss is assigned to the removal of crystal water as well as adsorbed water. There is about 30% weight loss between 240 °C and 500 °C, which is mainly due to the thermal decomposition of cyano group to release NO$_X$ and CO$_2$.[45] Notably, the weight of sample is increased slightly at 430 °C because of the chemical reaction in the thermal decomposition process. While the cyano group in Zn$_3$[Fe(CN)$_6$]$_2$ is constantly decomposed as the calcination temperature rises, Fe$_2$O$_3$ reacts with ZnO to generate ZnFe$_2$O$_4$.[28] After 500 °C, there is only a slight weight loss of the sample, and ZnO/ZnFe$_2$O$_4$ is fully formed. According to the TGA test of Zn$_3$[Fe(CN)$_6$]$_2$, the calcination temperature range of the self-sacrificial template method was set to be 420–

Scheme 1. Schematic illustration of the synthesis procedures for ZnO/ZnFe$_2$O$_4$ nanostructures prepared at different calcination temperatures and heating rates.
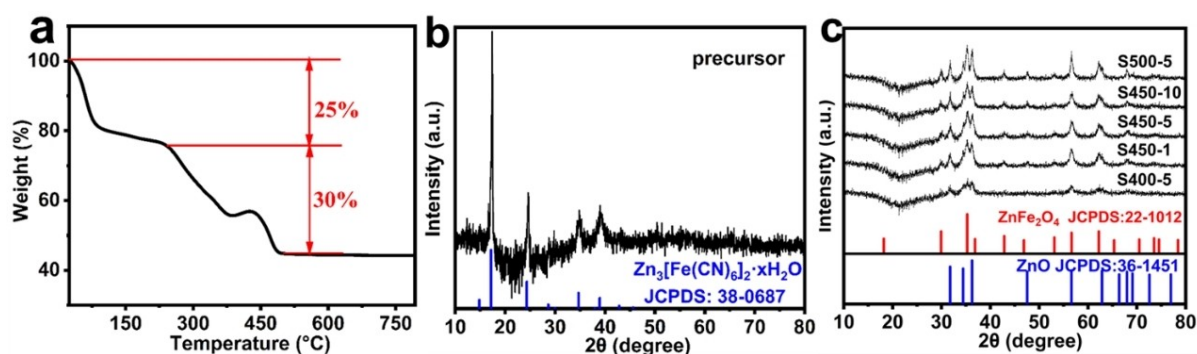

Figure 1. a) TGA curve and b) typical XRD pattern of Zn$_3$[Fe(CN)$_6$]$_2$; c) XRD patterns of calcined samples obtained from different calcination temperatures and heating rates.

800 °C. To analyze the differences in nanostructure and electrochemical properties in this temperature range, 400 °C, 450 °C, and 500 °C were selected as the calcination temperature, while the heating rate was set as 5 °C min^{-1}. In addition to the calcination temperature, the heating rate has a significant impact on the calcined sample. The samples were calcined at a heating rate of 1, 5, and 10 °C min^{-1} at a calcination temperature of 450 °C, to explore the effects of heating rate on the calcined products. To demonstrate the variation of the phase and crystallinity in the calcination process, XRD tests were carried on Zn$_3$[Fe(CN)$_6$]$_2$ and calcined samples. The XRD result of precursor verifies that the sample obtained by the precipitation of Zn(CH$_3$COO)$_2$·2H$_2$O and K$_3$Fe(CN)$_6$ at room temperature is Zn$_3$[Fe(CN)$_6$]$_2$·xH$_2$O (JCPDS: 38-0687) without other impurity phases, as shown in Figure 1(b). As exhibited in Figure 1(c), as the calcination temperature rises, the diffraction peaks of the samples gradually become much sharper and the intensity of the peaks increases continuously. Moreover, the

peak widths also decrease gradually. It shows that the disordered distribution of atoms or ions in the sample becomes more and more orderly and the crystallinity of the sample becomes better.[31] Because of the incomplete decomposition of cyano groups in the precursor at 400 °C, the XRD characteristic peaks of S400-5 are not obvious, indicating the low crystallinity. When the calcination temperature is raised to 450 °C and 500 °C, the cyano group in the precursor is further decomposed, and the transformation during the calcination process is completed. The crystallinity of the sample calcined at 450 °C (S450-5) is close to that of the sample calcined at 500 °C (S500-5). From XRD patterns, all diffraction peaks of samples could be well indexed as ZnO (JCPDS: 36-1451; space group: P63mc) and ZnFe$_2$O$_4$ (JCPDS: 22-1022; space group: Fd-3m).[46] This indicates that the calcined samples are ZnO/ZnFe$_2$O$_4$ composite materials without other impurity phases. As shown in XRD patterns (Figure 1c), the samples calcined at 450 °C with different heating rates have good crystallinity, and the peak

positions and intensity of the diffraction peaks are similar. It indicates that the samples calcined at different heating rates at 450 °C have same phases and similar crystallinity.

SEM and TEM measurements have been further carried to reveal the nanostructures of $Zn_3[Fe(CN)_6]_2$ and calcinated samples at different calcination temperatures and heating rates. Figure 2(a and d) shows that $Zn_3[Fe(CN)_6]_2$ obtained by coprecipitation at room temperature has a solid microsphere structure with the rough surface, good dispersibility, and homogeneous particle size of around 297 nm. The uniform size of the precursor is necessary for the self-sacrificial template

method. Figure 2(b, c and g) are typical SEM images of calcined samples at 400 °C, 450 °C, and 500 °C, respectively. The samples obtained by the self-sacrificial template method are all microspheres with a diameter of 200–500 nm. This indicates that the morphology of precursor does not change obviously during the high-temperature decomposition. When the temperature is raised to 500 °C, the morphology of S500-5 is severely damaged. From the damaged nanospheres, it can be found that the nanostructures of samples should be core-shell or hollow. To clarify the internal nanostructures of the obtained samples, TEM measurements were conducted on the obtained
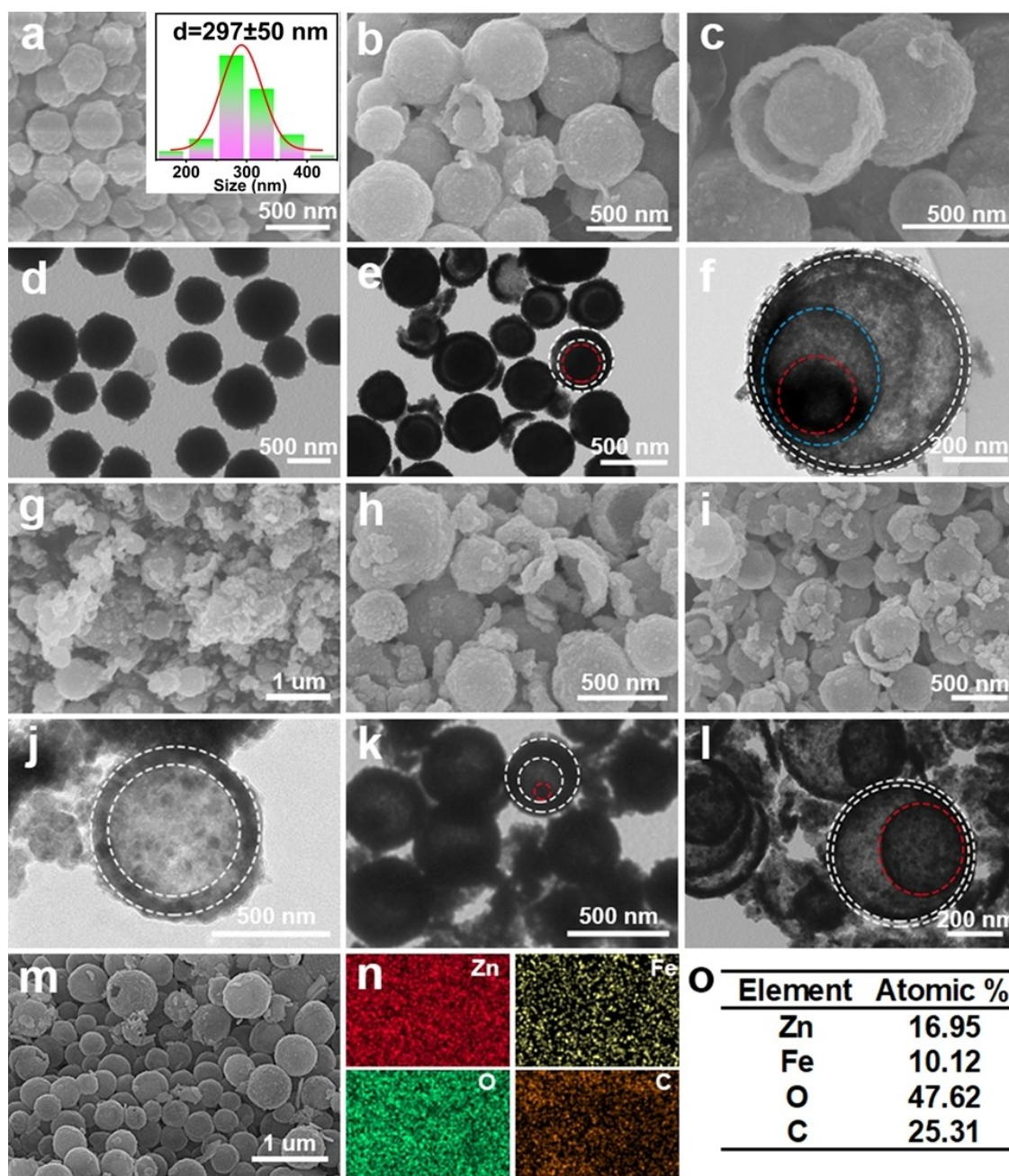

Figure 2. a) SEM images of $Zn_3[Fe(CN)_6]_2$, where the inset shows the particle size distribution; SEM images of b) S400-5 and c) S450-5; TEM images of d) $Zn_3[Fe(CN)_6]_2$, e) S400-5 and f) S450-5; SEM images of g) S500-5, h) S450-1 and i) S450-10; TEM images of j) S500-5, k) S450-1 and l) S450-10; m–o) SEM image and corresponding elemental analyses of S450-5.

Batteries & Supercaps

Research Article
doi.org/10.1002/batt.202200411

Chemistry Europe
European Chemical
Societies Publishing

samples, and results are shown in Figure 2(e, d and j). The TEM image shows that the sample S400-5 has a core-shell nanostructure with a thicker shell. Calcined at 450°C, the obtained sample S450-5 shows a core-double shell nanostructure, and the shell layer is obviously thinner. When the calcination temperature is increased to 500°C, the sample S500-5 has a hollow nanosphere structure with a thin shell and a large number of broken microspheres. The thickness of the shell is a key parameter of the core-shell nanostructure, and the thin shell is advantageous to promote the diffusion of Li ions.[47] With the rise of calcination temperature, the thickness of the shell layer becomes thinner obviously. A similar rule can be observed when calcined at different heating rates. The thickness of the shell decreases with the increasing of heating rate, as shown in Figure 2(k, f and l). The SEM images (Figure 2c, h and i) show that the samples calcined at 450°C at different heating rates have intact morphologies with only a few broken microspheres. The TEM images (Figure 2e and k) indicate that the sample S450-1 has the same core-shell nanostructures as S400-5. However, the core of S450-1 is much smaller than that of S400-5 because the cyano group decomposes severely at higher temperature, resulting in a larger shrinkage force. As the heating rate is raised to 10°C min^{-1} at 450°C, the sample S450-10 exhibits a double-shell nanostructure. Furthermore, the elemental distribution and content analysis of Zn, Fe, and O in sample S450-5 were revealed by EDS measurement. The SEM image and corresponding EDS results (Figure 2m–o) indicate that Zn, Fe, O, and C are evenly dispersed in the nanoparticles.[18] From the elemental ratio of the mapping pattern (Figure 2o), it can be accurately inferred that the mass ratio of ZnO to $ZnFe_2O_4$ in the sample is about 0.8. In order to

further determine the mass ratio of ZnO to $ZnFe_2O_4$ in the sample, ICP test was conducted for the sample S450-5, and the results are shown in Table S1. The mass ratio of Zn/Fe is 1.75, indicating that the mass ratio of ZnO to $ZnFe_2O_4$ in the product is 0.67, which is in good agreement with the previous EDS measurement results.[32] According to the BET test results (Figure S1), the sample S450-5 with core-double shell nanostructure has the highest specific surface area (37.36 m^{2}g^{-1}). The specific surface areas of samples S400-5 and S500-5 are 28.35 and 33.36 m^{2}g^{-1}, respectively. In addition, it can be found that the pores in above samples are mainly mesoporous, and the diameter of pores becomes larger with the increase of temperature.

XPS measurements (Figure 3) were conducted to study the composition as well as valence of sample S450-5. It can be observed from Figure 3(a) that the elements displayed in the sample are Zn, Fe, and O, and there are no other impurities, indicating that the synthetic method is appropriate and the product is pure. This is supported by the XRD and EDS results. As seen from the high-resolution Zn 2p spectrum (Figure 3b), the fitted peak located at 1021.0 eV corresponds to the 2p3/2 orbital of Zn, while the fitted peak at 1044.1 eV can be assigned to the 2p1/2 orbital. The characteristic peaks of Zn indicate that the existence of Zn in sample S450-5 is divalent. In terms of the spectrum for Fe 2p (Figure 3c), the fitted peaks at 710.5 and 712.4 eV could be well attributed to Fe 2p3/2, corresponding to the tetrahedral and octahedral sites in the crystal structure of $ZnFe_2O_4$, respectively. Meanwhile, other peaks at 732.2 eV, 724.3 eV, and 718.7 eV could be assigned to the satellite and Fe 2p1/2, respectively, which confirms the characteristic oxidation state of Fe^{3+} in the $ZnFe_2O_4$. Moreover, the O 1s spectrum
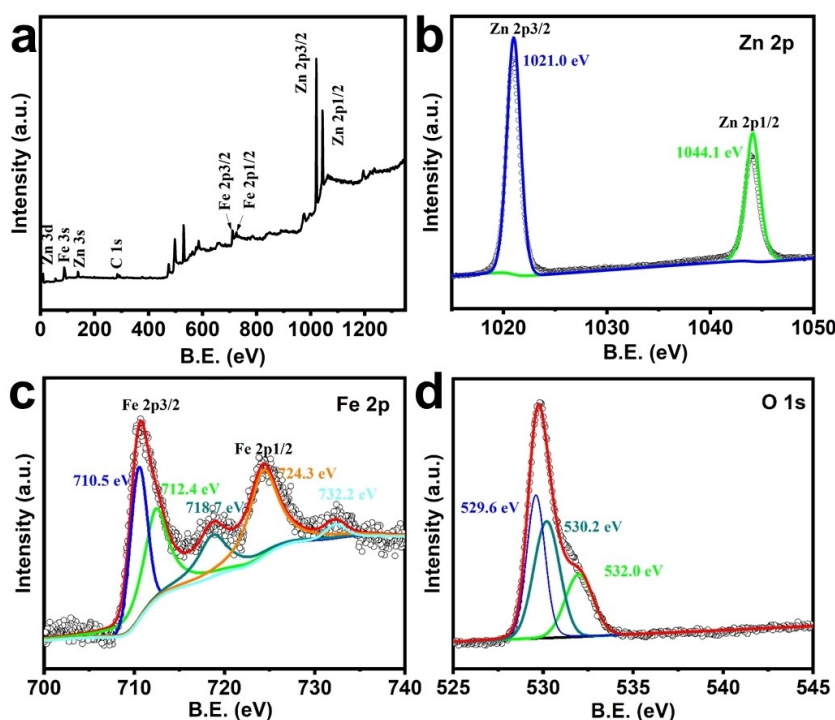

Figure 3. XPS survey spectrum of a) S450-5, b) Zn 2p, c) Fe 2p, and d) O 1s.

Batteries & Supercaps

Research Article
doi.org/10.1002/batt.202200411

Chemistry Europe
European Chemical
Societies Publishing

(Figure 3d) could be fitted into the following three parts: the peak at 529.6 eV is attributed to the typical lattice oxygen in the crystal structure. Another peak at 530.2 eV is rationally assigned to the existence of other oxygen components that are adsorbed on the sample surface. The weak peak at 532.0 eV originates from the existence of defect sites, which is caused by low oxygen coordination.[22,27,31]

Electrochemical performances

Driven by the special lithium-storage mechanism and core-shell nanostructures, the obtained $ZnO/ZnFe_2O_4$ shows good electrochemical performances.[48] The electrochemical activities of sample S450-5 were characterized by CV measurements (voltage window: 0.01 to 3.0 V; scan rate: 0.2 mV s^{-1}). As observed from the CV curves (Figure 4a) that the reduction peaks appear at 0.3, 0.58, 0.9, 1.23, and 1.46 V during the first discharging cycle. The peaks at 0.3 and 0.58 V reflect the reduction of $ZnO/ZnFe_2O_4$ and formation of Li_2O, respectively.[31,33] The peak at 0.9 V could be attributed to the
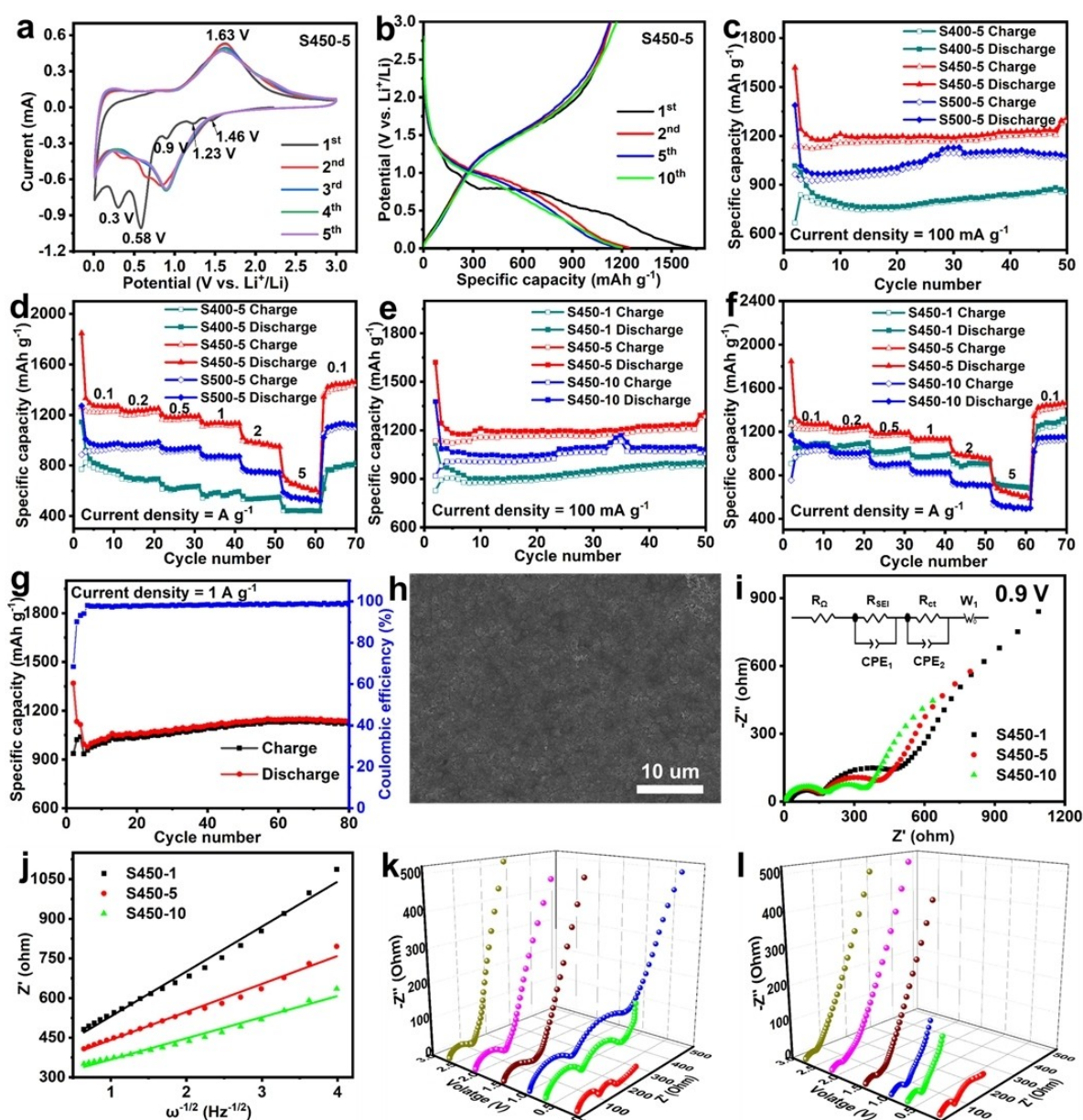

Figure 4. Electrochemical performances for LIBs: a) CV profiles and b) charge/discharge voltage curves of sample S450-5; c) cycling and d) rate performance of samples at different calcination temperatures; e) cycling and f) rate performances of samples at different heating rates; g) cycling performance at 1 A g^{-1} and h) SEM image of sample S450-5 after 80 cycles; i) Nyquist plots at different heating rates, where the inset shows the equivalent circuit diagram; j) corresponding variations between Z' and $\omega^{-1/2}$ at different heating rates; Nyquist plots of sample S450-5 k) before and l) after 10 cycles, respectively.

Batteries & Supercaps

Research Article
doi.org/10.1002/batt.202200411

Chemistry Europe
European Chemical
Societies Publishing

generation of SEI film. The reduction peaks at 1.23 and 1.46 V appear during the first discharging cycle but are invisible in the subsequent cycles, which might be due to the irreversible insertion of Li ions into $ZnFe_2O_4$ to form $Li_xZnFe_2O_4$.[27] In the second discharging cycle, the peaks at 0.34, 0.63, and 0.83 V are caused by the reduction reaction of Fe_2O_3 and ZnO. During the subsequent discharging cycles, the reduction peaks of Zn^{2+} and Fe^{3+} merge, yielding a reduction peak at 0.89 V. During the charging cycle, an obvious oxidation peak at 1.63 V can be well observed, corresponding to the oxidation of Zn^0 and Fe^0.[28] Apparently, the intensity of oxidation peak at 1.63 V gradually decreases in the subsequent cycles. The CV curves are completely overlapped from the third cycle, indicating that the core-shell nanostructured $ZnO/ZnFe_2O_4$ has reversible electrochemical properties.[49] The galvanostatic charging/discharging cycling (GCD) measurements were performed [voltage window: 0.01 to 3.0 V (versus Li/Li^+); current density: 100 mA g^{-1}] to further investigate the electrochemical properties in the lithiation/delithiation process. The typical charge/discharge voltage profiles of sample S450-5 for the 1st, 2nd, 5th, and 10th cycles are displayed in Figure 4(b). The discharge curve of the 1st cycle exhibits a small voltage plateau at 1 V, which however disappears in the subsequent cycles. This is because of the irreversible insertion of Li ions into the spinel-structured $ZnFe_2O_4$ in the 1st cycle, which matches well with CV measurement. A distinct discharge voltage plateau can be observed at 0.8 V. During the subsequent discharging process, the voltage plateau moves up to 0.9 V because of the structural recombination.[18,30] The specific capacities of charging/discharging in the first cycle are 1135 and 1620 mAh g^{-1}, respectively, and the initial Coulombic efficiency (CE) is 70%. The initial CE of sample S450-5 is much higher than other TMOs in the previous reports.[49] The specific capacity of sample S450-5 in this work is a bit larger than the theoretical capacity [≈ 1036 mAh g^{-1}, $(ZnO/ZnFe_2O_4) = 1072$ mAh g$^{-1} \times 60$ wt% $(ZnFe_2O_4) + 981$ mAh g$^{-1} \times 40$ wt% (ZnO)], which is caused by synergistic effects of ZnO and $ZnFe_2O_4$, high-content of nano-sized ZnO and additional formation of SEI film.[18] About 30% of irreversible losses in the 1st cycle could be mainly attributed to side reactions. In subsequent cycles, GCD curves remain stable, and the CE remains nearly 99%, indicating that the electrochemical reactions of the core-shell nanostructure are highly reversible.[30] Notably, the specific capacity of the sample S450-5 for the 10th cycle is much higher than that for the 5th cycle, which is caused by the activation of active materials. The cycling performances of samples prepared at different calcina-

tion temperatures and heating rates are illustrated in Figure 4(c and e). Compared with other samples, the sample S450-5 still keeps an excellent discharge specific capacity of 1310 mAh g^{-1} at 0.1 A g^{-1} after 50 cycles. In addition, the initial discharge capacity of sample S450-5 is higher than other samples because the core-double shell nanostructure provides more active sites.[50–52] The initial discharge capacity of S400-5 is a bit lower than other samples because the thick shell prevents the inner core from fully participating in the electrochemical reaction. It is noted that the reversible capacity of $ZnO/ZnFe_2O_4$ is enhanced to varying degrees after cycles due to the generation of polymer gel-like films during kinetic activation.[25] The rate performance of the sample is the key indicator for commercial applications.[53,54] Figure 4(d and f) shows the rate performance of as-obtained $ZnO/ZnFe_2O_4$ samples. The discharge capacities of sample S450-5 are 1270, 1235, 1180, 1136, 982, 635, and 1442 mAh g^{-1}, at 0.1, 0.2, 0.5, 1, 2, 5, and 0.1 A g^{-1}, respectively. In case the current density is raised from 0.1 to 5 A g^{-1}, about 50% of capacity is maintained. Compared with samples prepared at other calcination temperatures and heating rates, the sample S450-5 has excellent rate capability. Because of the activation of $ZnO/ZnFe_2O_4$, the discharge capacity becomes higher than before as the current density recovers to 0.1 A g^{-1}. Notably, the discharge capacity of S450-5 still can reach at 635 mAh g^{-1} at 5 A g^{-1}, which is significantly larger than that of commercial graphite-based anodes. Thus, it is believed that $ZnO/ZnFe_2O_4$ has a promising commercial application prospect. At the same time, it is also proved that the unique core-double shell heterostructures are good for accelerating the insertion/extraction of Li ions and shortening the diffusion pathway of Li-ions. The cycling performance of S450-5 at 1 A g^{-1} is illustrated in Figure 4(g), and the charge/discharge capacity also keeps 1120/1137 mAh g^{-1} after 80 cycles. This is another significant advantage when compared with previously reported materials in Table 1. The SEM image of S450-5 after 80 cycles is shown in Figure 4(h), the surface of active material is uniform and there is no cracking. At high current densities, the discharge capacity keeps increasing, which also verifies that the active material is continuously activated during cycles. As shown in Figure 5, sample S450-5 can exhibit good electrochemical performances because the core-double shell nanostructure can significantly relieve the volume expansion in the intercalation/delithiation processes.

To analyze the kinetic performance of core-shell nanostructures during cycles, EIS measurements were conducted on the obtained $ZnO/ZnFe_2O_4$ samples. The EIS results of calcined

Table 1. Comparison of the cycling performance of $ZnFe_2O_4$ and $ZnFe_2O_4$-derived materials.

Electrode material	Morphology	Current density [mA g^{-1}]	Cycle number	Specific capacity [mAh g^{-1}]	Reference
$ZnO/ZnFe_2O_4$	core-double shell	1000	80	1137	This work
$ZnO/ZnFe_2O_4$@C	core-shell	500	60	893	[31]
$ZnO/ZnFe_2O_4$/N-doped C	hollow micro-polyhedrons	200	100	1000	[46]
$ZnFe_2O_4$ nanosheet/reduced graphene oxide (rGO)	two-dimensional holey	500	100	1022	[22]
$ZnFe_2O_4$	hollow	200	120	1101	[55]
$ZnFe_2O_4$@rGO	core-shell	1000	100	668	[56]
$ZnFe_2O_4$ carbonaceous	micron-sized particles	500	100	870	[57]

Batteries & Supercaps

Research Article
doi.org/10.1002/batt.202200411

Chemistry
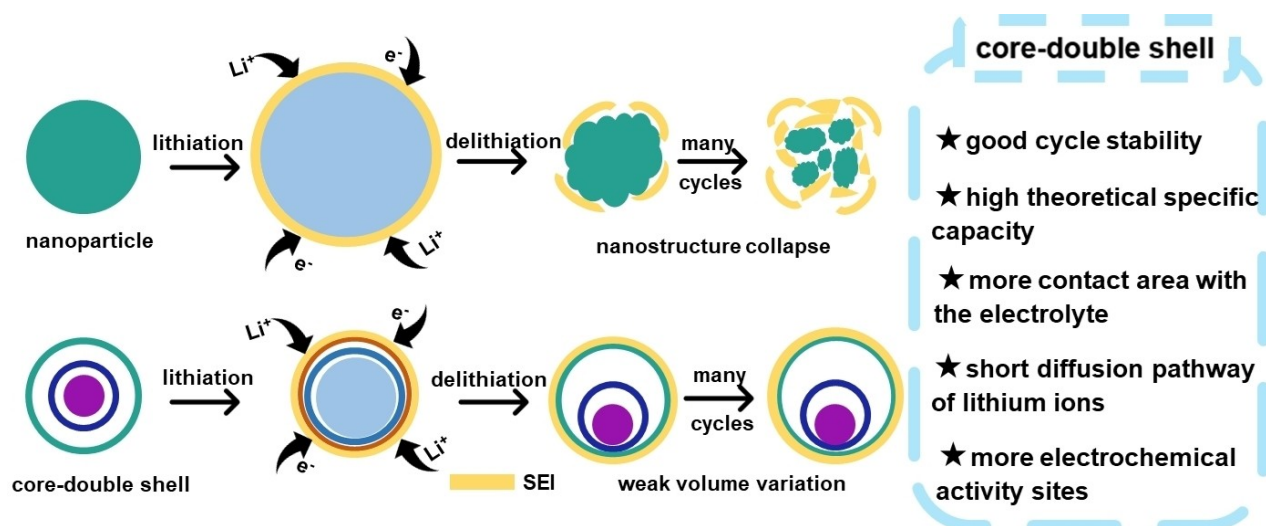Europe
European Chemical
Societies Publishing

Figure 5. Schematic illustration of solid nanoparticles and core-double shell nanostructures in the lithiation/delithiation processes.

samples at different heating rates have been illustrated in Figure 4(i). There are two obvious semicircles in the high-frequency region as well as middle frequency region, which correspond to the impedance of electrolyte and resistance of SEI film, respectively.[58] The differences between samples in the low-frequency region are due to differences in the solid-state diffusion of lithium ions at different nanostructures. According to the equations:[59]

$$D_{Li^+} = \frac{R^2 T^2}{2A^2 n^4 F^4 C^2 \sigma^2} \text{ and } Z' = \sigma \omega^{-0.5},$$

the slope of the line in Figure 4(j) is inversely proportional to the diffusion coefficient. As the thickness of the shell becomes thinner, the diffusion coefficient of Li ions becomes larger. According to the above formula, the Li-ion diffusion coefficients of S450-1, S450-5, and S450-10 are 1.26×10^{-17}, 3.23×10^{-17}, and 5.81×10^{-17} cm^{2}s^{-1}, respectively. From EIS results of sample S450-5 before cycling test (Figure 4k), an obvious semicircle appears in the middle frequency region of 0.9 V, indicating that a large impedance appears at the electrolyte-electrode inter-face at this time, corresponding to the generation of SEI film. It also confirms what the CV curves reflect. When the discharge voltage drops to 0.6 and 0.05 V, the impedance in the middle frequency region also drops, indicating that the generation of SEI is a dynamic process during the first cycle. Compared with the EIS results before the first cycle, the impedance in the middle frequency region is significantly reduced after 10 cycles, indicating that SEI film has been formed, as demonstrated in Figure S2. Moreover, the lithium-ions diffusion coefficient of the sample S450-5 increases from 3.23×10^{-17} to 5.62×10^{-16} cm^{2}s^{-1} after 10 cycles, which confirms the generation of SEI film, as illustrated in Figure S3. Figure 4(l) shows that during the discharging process, the impedance in the middle frequency region is basically similar after 10 cycles, which confirms that the SEI film of the unique core-double shell nanostructure tends to be stable.[60–64]

Based on the abundant potassium resources, more and more researchers have begun to develop PIBs.[65] Because of the unique core-double shell nanostructure and synergistic effects of ZnO and ZnFe$_2$O$_4$, the ZnO/ZnFe$_2$O$_4$ not only has good performances for LIBs but also possesses great potential in PIBs.[66] The GCD measurement uses the potassium metal as counter and reference electrodes at 100 mA g^{-1} to explore the properties of potassium-storage. The GCD curve (Figure 6a) shows that the initial reversible specific capacity and initial CE are 459 mAh g^{-1}, and 52.02%, respectively. Due to the large ionic radius of potassium ion, ZnO/ZnFe$_2$O$_4$ has a lower specific capacity as PIB anodes than LIB anodes. However, when used as PIB anodes, ZnO/ZnFe$_2$O$_4$ is continuously activated in the first 50 cycles, and the discharge capacity has gradually risen to 224 mAh g^{-1} (at 50 cycles). As the increase of cycle numbers, the core-double shell nanostructured ZnO/ZnFe$_2$O$_4$ is fully activated and the specific capacity remains at 217 mAh g^{-1} after 400 cycles. The rate performance of S450-5 is revealed in Figure 6(b). The discharge capacities of sample S450-5 at 0.1, 0.2, 0.5, 1, 2, and 5 A g^{-1} are 239, 182, 126, 92, 60 and 31 mAh g^{-1}, respectively. Note that as the current density is reverted to 0.1 A g^{-1}, the discharge capacity could recover to 187 mAh g^{-1}. This shows that the core-double shell nano-structured ZnO/ZnFe$_2$O$_4$ has excellent rate performance as PIB anodes. Figure 6(c) displays the charge/discharge voltage curves of sample S450-5 as PIB anodes for different cycles. The potassium-storage performances of the sample experience a rapid capacity decay after the first cycle and remain stable from the second cycle. Similar to LIBs, the irreversible capacity of the first cycle is also due to the generation of SEI film and Fe$_2$O$_3$. It indicates that ZnO/ZnFe$_2$O$_4$ has excellent cycling stability as anodes for PIB. The potassium-storage mechanism of sample S450-5 was investigated by the CV measurement (voltage window: 0.01–3.0 V (versus K/K$^+$); scan rate: 0.2 mV s^{-1}). CV curves of core-double shell nanostructured ZnO/ZnFe$_2$O$_4$ for the first five cycles are demonstrated in Figure 6(d). The peaks at 0.84 and 0.12 V are caused by SEI film and conversion
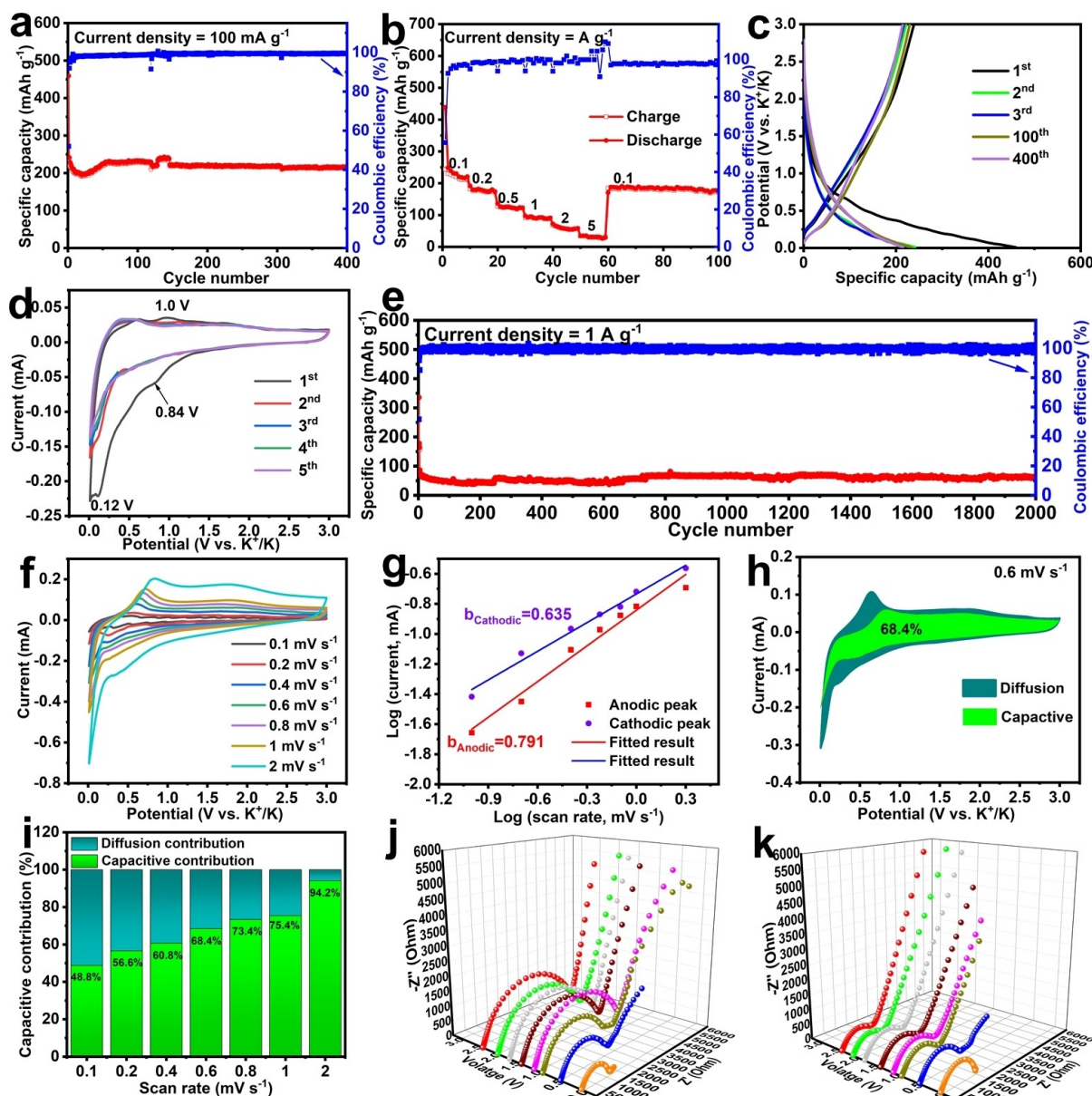
Figure 6. Electrochemical performances of sample S450-5 for PIBs: a) cycling performance; b) rate performance; c) charge/discharge voltage curves at 0.1 A g^{-1}; d) CV profiles at a scan rate of 0.2 mV s^{-1}; e) cycling performance at 1 A g^{-1}; f) CV profiles; g) the relationship between log(current) and log(scan rate); h) the capacitive contribution of CV profiles at 0.6 mV s^{-1}; i) the capacitive contribution at various scan rates; the Nyquist plots of the sample S450-5 j) before and k) after 10 cycles.

reaction in the 1st cycle.[66] The oxidation peak at 1.0 V is due to K$^+$ extraction. In the subsequent cycles, no obvious peaks are observed, showing the outstanding reversibility of the charging/discharging process.[67,68] As shown in Figure 6(e), even after 2000 cycles at 1 A g^{-1}, the sample S450-5 could well keep a capacity of 60 mAh g^{-1}.

Figure 6(f) shows CV measurements at various scan rates ranging from 0.1 to 2 mV s^{-1} to explore the kinetic properties and the potassium-storage mechanism of the core-double shell nanostructured ZnO/ZnFe$_2$O$_4$ as PIB anodes. The general shape of CV curves does not change obviously under different scan rates, and the intensity of the oxidation peak increases as the scan rate increases. Furthermore, according to the equation:[69]

$i = av^b$ (i: peak current; v: scan rate; a and b: constants), the magnitude of the b value could analyze the diffusion behavior of potassium ions. When $b = 1$, capacitive behavior controls the diffusion of potassium ions. And when $b = 0.5$, diffusion behavior controls the diffusion of potassium ions. As depicted in Figure 6(g), the b value of anodic and cathodic peaks for ZnO/ZnFe$_2$O$_4$ electrode are 0.791 and 0.635, respectively, which proves that the diffusion of potassium ions in this electrode is controlled by the capacitive behavior and the diffusion behavior.[70] The capacitive contribution of S450-5 can reach 68.4% at 0.6 mV s^{-1}, as illustrated in Figure 6(h). The capacitance contribution ratios are 48.8%, 56.6%, 60.8%, 68.4%, 73.4%, 75.4%, and 94.2% at scan rates from 0.1 to 2 mV s^{-1}, as

illustrated in Figure 6(i). It could be clearly found that the capacitance contribution increases significantly, as the scan rate is increased. When the scan rate is raised to 2 mV s^{-1}, the diffusion of potassium ions is almost dominated by capacitive behavior. Therefore, when the ZnO/ZnFe$_2$O$_4$ with conversion reaction and alloying/dealloying reaction type is used as PIB anodes, the potassium ions cannot fully react with the electrode material at high current density, thus causing low reversible capacity. The EIS measurements were performed on the core-double shell nanostructured ZnO/ZnFe$_2$O$_4$ before and after 10 cycles, and the corresponding results are demonstrated in Figure 6(j and k). The interphase charge-transfer process is represented by a semicircle in the middle-high frequency area, while the K$^+$ diffusion rate is represented by a slanting line in the low-frequency area. During the first potassium-ion intercalation, with the voltage decreasing, SEI film begins to form gradually, and the interfacial transfer resistance decreases continuously. After 10 cycles, SEI film is almost formed, so the impedance in the middle-high frequency region does not change significantly during the potassium-ion intercalation process.

To further analyze the potassium-storage mechanism of ZnO/ZnFe$_2$O$_4$, XPS and HRTEM were conducted on the core-double shell nanostructured ZnO/ZnFe$_2$O$_4$ after cycles. In the K 2p spectrum (Figure 7b), the corresponding K 2p3/2 and K 2p1/2 peaks could all be attributed to K$_2$CO$_3$ in the SEI film.[71] Compared with the electrode discharging to 0.01 V (Table S2), the content of potassium atoms on the surface of the electrode after charging to 3 V is significantly lower, which is because of the partial decomposition of SEI film during the charging process. In addition, from the fitted results of the O 1s spectrum (Figure 7c), it could be found that the peak of O−Fe at 3 V is significantly higher than that at 0.01 V, which is due to the oxidation of metallic Fe to Fe$_2$O$_3$. While other peaks of O are mainly from SEI film on the surface, such as polyester, K$_2$CO$_3$, etc.[72] The peaks of Fe 2p in the fully discharged state are significantly weaker than that in the fully charged state in Figure 7(d), which could be attributed to the conversion reaction of potassium-ion intercalation to generate metallic Fe. When charging to 3 V, the Fe 2p peak returns to a similar intensity to that of ZnO/ZnFe$_2$O$_4$ before cycle, indicating that the potassium-storage of ZnO/ZnFe$_2$O$_4$ is highly reversible.
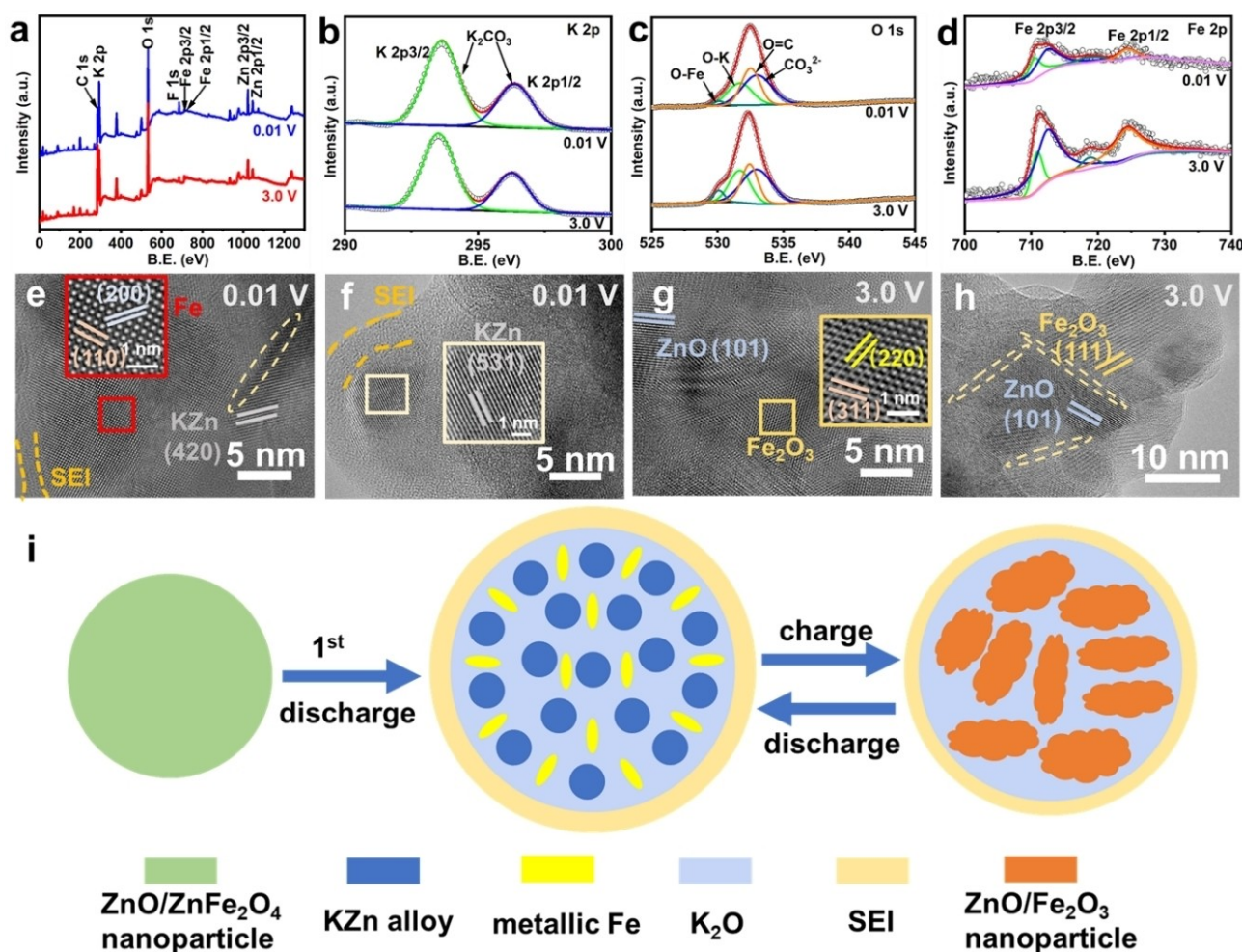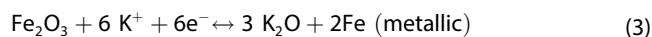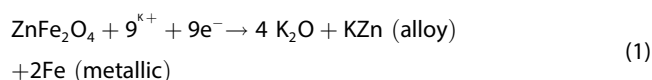

Figure 7. XPS survey spectra of S450-5 after discharging to 0.01 V and charging to a) 3 V, b) K 2p, (c) O 1s, and d) Fe 2p; e, f) HRTEM profiles of S450-5 after discharging to 0.01 V and g, h) charging to 3.0 V; i) schematic illustration of the electrochemical reactions of ZnO/ZnFe$_2$O$_4$ as PIB anodes.

Batteries & Supercaps

Research Article
doi.org/10.1002/batt.202200411

Chemistry
Europe

European Chemical
Societies Publishing

The typical HRTEM images of electrode after discharging to 0.01 V are displayed in Figure 7(e and f). The clear lattice fringes in Figure 7(e and f) can be matched with the corresponding crystal planes of metallic Fe and KZn.[73] This shows that ZnO/ZnFe$_2$O$_4$ also undergoes conversion reaction and alloying/dealloying reaction when it is used as PIB anodes and generates KZn alloy and metallic Fe in the fully discharged state. In addition, the surface of electrode is covered with a uniform and stable SEI film in the fully discharged state, meeting well with the previous electrochemical tests and XPS analysis results. Through the HRTEM image of electrode fully charged to 3 V (Figure 7g and h), KZn alloy and metallic Fe are oxidized to ZnO and Fe$_2$O$_3$. This proves that the potassium-storage capacity of the core-double shell nanostructured ZnO/ZnFe$_2$O$_4$ is highly reversible. Note that no matter when fully charged or fully discharged, there are obvious crystal boundaries between the crystal grains. It can be observed from Figure 7(h) that the size of the crystal grain is as small as about 10 nm, which is beneficial to lessen the volume expansion of TMOs, leading to the good cycling stability of ZnO/ZnFe$_2$O$_4$ as PIB anodes. According to the above analysis and previous related studies,[74–76] electrochemical reactions of ZnO/ZnFe$_2$O$_4$ as PIB anodes (Figure 7i) can be described by the following equations:

$$ZnFe_2O_4 + 9^{K^+} + 9e^- \rightarrow 4\ K_2O + KZn\ (alloy) + 2Fe\ (metallic) \tag{1}$$

$$ZnO + 3\ K^+ + 3e^- \leftrightarrow K_2O + KZn\ (alloy) \tag{2}$$

$$Fe_2O_3 + 6\ K^+ + 6e^- \leftrightarrow 3\ K_2O + 2Fe\ (metallic) \tag{3}$$

Since the first discharging process of ZnFe$_2$O$_4$ is irreversible, the first discharging process of ZnO/ZnFe$_2$O$_4$ could be assigned to the reaction [Equations (I) and (II)], and the subsequent charging/discharging processes could be assigned to the reaction [Equations (II) and (III)].

Conclusion

In summary, we have successfully prepared ZnO/ZnFe$_2$O$_4$ core-shell nanostructures using Prussian blue analogue (i.e., Zn$_3$[Fe(CN)$_6$]$_2$) as the self-sacrificing template. The generation of the core-shell nanostructure could be attributed to the Kirkendall effect in the process of calcining the Zn$_3$[Fe(CN)$_6$]$_2$. By controlling the calcination temperatures and heating rates, different types of core-shell heterostructures could be designed and obtained. When the calcination temperature of the precursor is 450 °C and heating rate is 5 °C min^{-1}, the calcined sample exhibits a core-double shell nanostructure. Compared with other nanostructures, this unique core-double shell nanostructure could expose more electrochemical active sites and enlarge the specific surface area of ZnO/ZnFe$_2$O$_4$. The internal cavity of the core-double shell nanostructure can remarkably relieve the volume expansion during the cycles. As a result, the core-double shell nanostructured ZnO/ZnFe$_2$O$_4$ shows a reversible capacity as high as 1310 mAh g^{-1} at 0.1 A g^{-1} after 50 cycles and 1137 mAh g^{-1} at 1 A g^{-1} after 80 cycles as LIB anodes. In addition, it also has great potential in PIBs, showing a discharge capacity of 217 mAh g^{-1} at 0.1 A g^{-1} after 400 cycles. The strategy of this work opens a novel avenue for the commercial application of TMOs.

Experimental Section

Synthesis of ZnO/ZnFe$_2$O$_4$ core-shell nanospheres

1 mmol Zn(CH$_3$COO)$_2 \cdot$ 2H$_2$O and 0.5 g polyvinylpyrrolidone (PVP, K29-32, M_W = 58000) were dissolved in deionized (DI) water (25 mL) to make solution A. 1 mmol K$_3$Fe(CN)$_6$ was added into 25 mL of DI water to make solution B. Next, solution B was then mixed with solution A quickly. The mixture was then aged for 24 h at 25 °C, after stirring for 30 min. Then, the obtained precipitate was collected, washed several times, and dried to obtain the Zn$_3$[Fe(CN)$_6$]$_2$ precursor. In order to obtain a core-double shell nanostructured ZnO/ZnFe$_2$O$_4$ sample (S450-5), the precursor was calcined at 450 °C in air for 2 h (heating rate: 5 °C min^{-1}). To investigate the morphologies, nanostructures, and properties of ZnO/ZnFe$_2$O$_4$ at different temperatures and heating rates, the calcination temperatures and heating rates of the samples were set as 400 °C–5 °C min^{-1} (S400-5), 500 °C–5 °C min^{-1} (S500-5), 450 °C–1 °C min^{-1} (S450-1) and 450 °C–10 °C min^{-1} (S450-10).

Material characterization

The thermogravimetric analysis (TGA, TGA550) was used to determine the weight loss accompanied with the decomposition of Zn$_3$[Fe(CN)$_6$]$_2$ (heating rate: 5 °C min^{-1}; temperature range: 30–800 °C; gas atmosphere: air). To analyze changes in phase and crystallinity, the Zn$_3$[Fe(CN)$_6$]$_2$ precursor and annealed samples were tested by X-ray diffractometer (XRD, Bruker D8). The morphology and nanostructures of samples were studied by transmission electron microscopy (TEM, JEOL-2010) as well as scanning electron microscopy (SEM, HITACHI-SU8220) with energy dispersive X-ray spectrometer (EDS). Ion concentrations were analyzed by inductively coupled plasma (ICP, Avio200). The surface area and pore size of samples were analyzed by Brunauer-Emmett-Teller (BET, ASAP 2020). X-ray photoelectron spectroscopy (XPS, ESCALAB 250Xi) was used to measure the chemical bonding states of calcined samples and sample S450-5 after cycling tests. The sample S450-5 before and after cycling tests were further characterized by high-resolution TEM (HRTEM, JEM–F200).

Electrochemical test

Electrodes were fabricated by mixing ZnO/ZnFe$_2$O$_4$ samples (60 wt.%), sodium carboxymethyl cellulose (CMC, 10 wt.%), and commercial acetylene black (30 wt.%) on the commercial copper foil and drying at 80 °C for 24 h. The mass loading of active material in electrodes was between 0.6 and 1.0 mg cm^{-2}. Coin cells were assembled in the Ar atmosphere. In this work, 1 M LiPF$_6$ in a mixture solvent of ethylene carbonate, dimethyl carbonate, and ethyl methyl carbonate (EC/DMC/EMC 1:1:1 in volume) was used as the LIB electrolyte and 1 M KFSI in a mixture solvent of ethylene carbonate and diethyl carbonate (EC/DEC 1:1 in volume) was used as the PIB electrolyte. The cycling and rate performances were tested by the battery measurement system (CT2001 A, China) with a potential range of 0.01–3.0 V. Electrochemical impedance (EIS)

and cyclic voltammetry (CV) tests were conducted by electrochemical workstations (CHI660E, China).

Conflict of Interest

The authors declare no conflict of interest.

Data Availability Statement

Research data are not shared.

[1] B. Dunn, H. Kamath, J. M. Tarascon, *Science* **2011**, *334*, 928.
[2] G. Zhou, F. Li, H.-M. Cheng, *Energy Environ. Sci.* **2014**, *7*, 1307.
[3] X. Wang, X. Lu, B. Liu, D. Chen, Y. Tong, G. Shen, *Adv. Mater.* **2014**, *26*, 4763.
[4] R. Raccichini, A. Varzi, S. Passerini, B. Scrosati, *Nat. Mater.* **2015**, *14*, 271.
[5] C. Z. Ke, R. W. Shao, Y. G. Zhang, Z. F. Sun, S. Qi, H. H. Zhang, M. Li, Z. L. Chen, Y. S. Wang, B. S. Sa, H. C. Lin, H. D. Liu, M. S. Wang, S. Q. Chen, Q. B. Zhang, *Adv. Funct. Mater.* **2022**, *32*, 2205635.
[6] R. Cai, L. Bao, W. Zhang, W. Xia, C. Sun, W. Dong, X. Chang, Z. Hua, R. Shao, T. Fukuda, Z. Sun, H. Liu, Q. Zhang, F. Xu, L. Dong, *InfoMat* **2022**, DOI: 10.1002/inf2.12364.
[7] M. T. Cai, H. H. Zhang, Y. G. Zhang, B. S. Xiao, L. Wang, M. Li, Y. Wu, B. S. Sa, H. G. Liao, L. Zhang, S. Q. Chen, D. L. Peng, M. S. Wang, Q. B. Zhang, *Sci. Bull.* **2022**, *67*, 933.
[8] S. Goriparti, E. Miele, F. De Angelis, E. Di Fabrizio, R. Proietti Zaccaria, C. Capiglia, *J. Power Sources* **2014**, *257*, 421.
[9] G. D. Park, J. S. Park, J. K. Kim, Y. C. Kang, *Adv. Energy Mater.* **2021**, *11*, 2003058.
[10] R. Schmuch, R. Wagner, G. Hörpel, T. Placke, M. Winter, *Nat. Energy* **2018**, *3*, 267.
[11] Y. Zhao, X. Li, B. Yan, D. Xiong, D. Li, S. Lawes, X. Sun, *Adv. Energy Mater.* **2016**, *6*, 1502175.
[12] X. Y. Feng, H. H. Wu, B. Gao, M. Swietoslawski, X. He, Q. B. Zhang, *Nano Res.* **2022**, *15*, 352.
[13] C. Z. Ke, F. Liu, Z. M. Zheng, H. H. Zhang, M. T. Cai, M. Li, Q. Z. Yan, H. X. Chen, Q. B. Zhang, *Rare Met.* **2021**, *40*, 1347.
[14] C. Yuan, H. B. Wu, Y. Xie, X. W. Lou, *Angew. Chem. Int. Ed. Engl.* **2014**, *53*, 1488.
[15] M. Zheng, H. Tang, L. Li, Q. Hu, L. Zhang, H. Xue, H. Pang, *Adv. Sci.* **2018**, *5*, 1700592.
[16] H. Ye, Z. Gzheng, X. Yang, D. Zhang, Y. Zhang, S. Yan, L. You, S. Hou, Z. Huang, *J. Electroanal. Chem.* **2021**, *898*, 115652.
[17] Y. Sharma, N. Sharma, G. V. S. Rao, B. V. R. Chowdari, *Electrochim. Acta* **2008**, *53*, 2380.
[18] L. Hou, L. Lian, L. Zhang, G. Pang, C. Yuan, X. Zhang, *Adv. Funct. Mater.* **2015**, *25*, 238.
[19] M. Chen, D. Liu, Y. Deng, W. Fu, H. Zou, F. Liang, *Ceram. Int.* **2017**, *43*, 16027.
[20] Y. Deng, Q. Zhang, S. Tang, L. Zhang, S. Deng, Z. Shi, G. Chen, *Chem. Commun.* **2011**, *47*, 6828.
[21] X. Lu, A. Xie, Y. Zhang, H. Zhong, X. Xu, H. Liu, Q. Xie, *Electrochim. Acta* **2017**, *249*, 79.
[22] W. Yao, Z. Xu, X. Xu, Y. Xie, W. Qiu, J. Xu, D. Zhang, *Electrochim. Acta* **2018**, *292*, 390.
[23] Y. Ding, Y. Yang, H. Shao, *Electrochim. Acta* **2011**, *56*, 9433.
[24] X. Guo, X. Lu, X. Fang, Y. Mao, Z. Wang, L. Chen, X. Xu, H. Yang, Y. Liu, *Electrochem. Commun.* **2010**, *12*, 847.
[25] J. M. Won, S. H. Choi, Y. J. Hong, Y. N. Ko, Y. C. Kang, *Sci. Rep.* **2014**, *4*, 5857.
[26] Z. Xing, Z. Ju, J. Yang, H. Xu, Y. Qian, *Nano Res.* **2012**, *5*, 477.
[27] L. Zhang, T. Wei, J. Yue, L. Sheng, Z. Jiang, D. Yang, L. Yuan, Z. Fan, *J. Mater. Chem. A* **2017**, *5*, 11188.
[28] X. Yang, X. Xue, Q. Yang, R. Yuan, W. Kang, C.-S. Lee, *Chem. Eng. J.* **2017**, *308*, 340.
[29] B. Y. Guan, X. Y. Yu, H. B. Wu, X. W. D. Lou, *Adv. Mater.* **2017**, *29*, 1703614.
[30] B. Jiang, C. Han, B. Li, Y. He, Z. Lin, *ACS Nano* **2016**, *10*, 2728.
[31] C. Yuan, H. Cao, S. Zhu, H. Hua, L. Hou, *J. Mater. Chem. A* **2015**, *3*, 20389.
[32] F. Zou, X. Hu, Z. Li, L. Qie, C. Hu, R. Zeng, Y. Jiang, Y. Huang, *Adv. Mater.* **2014**, *26*, 6622.
[33] S. Fang, D. Bresser, S. Passerini, *Adv. Energy Mater.* **2019**, *10*, 1902485.
[34] L. Hou, R. Bao, Y. Zhang, X. Sun, J. Zhang, H. Dou, X. Zhang, C. Yuan, *J. Mater. Chem. A* **2018**, *6*, 17947.
[35] X. Sun, X. Zhang, L. Zhou, X. Huang, C. Yu, *Small* **2016**, *12*, 3732.
[36] X. Wang, J. Feng, Y. Bai, Q. Zhang, Y. Yin, *Chem. Rev.* **2016**, *116*, 10983.
[37] N. Liu, Z. Lu, J. Zhao, M. T. Mcdowell, H. W. Lee, W. Zhao, Y. Cui, *Nat. Nanotechnol.* **2014**, *9*, 187.
[38] C. Nie, Y. Deng, H. Ren, Y. Zhao, X. Ji, L. Zhu, Z. Xing, J. Liu, Z. Ju, *CrystEngComm* **2019**, *21*, 5508.
[39] W. Xia, A. Mahmood, R. Zou, Q. Xu, *Energy Environ. Sci.* **2015**, *8*, 1837.
[40] J. Chen, F. Jiang, Y. Yin, *Acc. Chem. Res.* **2021**, *54*, 1168.
[41] Y. D. Yin, R. M. Rioux, C. K. Erdonmez, S. Hughes, G. A. Somorjai, A. P. Alivisatos, *Science* **2004**, *304*, 711.
[42] L. Shen, L. Yu, X. Y. Yu, X. Zhang, X. W. Lou, *Angew. Chem. Int. Ed. Engl.* **2015**, *54*, 1868.
[43] G. Zhang, L. Yu, H. B. Wu, H. E. Hoster, X. W. Lou, *Adv. Mater.* **2012**, *24*, 4609.
[44] J. Li, S. Xiong, X. Li, Y. Qian, *Nanoscale* **2013**, *5*, 2045.
[45] W. Ye, L. Yu, M. Sun, G. Cheng, S. Fu, S. Peng, S. Han, X. Yang, *Electrochim. Acta* **2019**, *319*, 237.
[46] Y. Ma, Y. Ma, D. Geiger, U. Kaiser, H. Zhang, G.-T. Kim, T. Diemant, R. J. Behm, A. Varzi, S. Passerini, *Nano Energy* **2017**, *42*, 341.
[47] D. Luo, Y. P. Deng, X. Wang, G. Li, J. Wu, J. Fu, W. Lei, R. Liang, Y. Liu, Y. Ding, A. Yu, Z. Chen, *ACS Nano* **2017**, *11*, 11521.
[48] H. Yu, H. Fan, B. Yadian, H. Tan, W. Liu, H. H. Hng, Y. Huang, Q. Yan, *ACS Appl. Mater. Interfaces* **2015**, *7*, 26751.
[49] J. Jiang, Y. Li, J. Liu, X. Huang, C. Yuan, X. W. Lou, *Adv. Mater.* **2012**, *24*, 5166.
[50] A. S. Hameed, H. Bahiraei, M. V. Reddy, M. Z. Shoushtari, J. J. Vittal, C. K. Ong, B. V. Chowdari, *ACS Appl. Mater. Interfaces* **2014**, *6*, 10744.
[51] Y. Wu, J. Meng, Q. Li, C. Niu, X. Wang, W. Yang, W. Li, L. Mai, *Nano Res.* **2017**, *10*, 2364.
[52] W. Yin, Y. Shen, F. Zou, X. Hu, B. Chi, Y. Huang, *ACS Appl. Mater. Interfaces* **2015**, *7*, 4947.
[53] P. F. Teh, Y. Sharma, S. S. Pramana, M. Srinivasan, *J. Mater. Chem.* **2011**, *21*, 14999.
[54] D. Yang, J. Feng, L. Jiang, X. Wu, L. Sheng, Y. Jiang, T. Wei, Z. Fan, *Adv. Funct. Mater.* **2015**, *25*, 7080.
[55] M. Yu, M. Huang, K. Wang, X. Han, M. Wang, Y. Zhu, L. Liu, *Appl. Surf. Sci.* **2018**, *462*, 955.
[56] J. Zhu, D. Wang, D. Chen, B. Song, Y. Li, F. Liu, J. Chen, *J. Solid State Electrochem.* **2020**, *848*, 156593.
[57] S. Das, D. Das, A. Mitra, S. Jena, A. Bhattacharya, S. B. Majumder, *Mater. Lett.* **2021**, *301*, 130265.
[58] X. Jiang, H. Liu, J. Song, C. Yin, H. Xu, *J. Mater. Chem. A* **2016**, *4*, 16205.
[59] D. Zhang, J. Zhang, Z. Yang, X. Ren, H. Mao, X. Yang, J. Yang, Y. Qian, *Chem. Commun.* **2017**, *53*, 10556.
[60] W. Guo, W. Sun, L. P. Lv, S. Kong, Y. Wang, *ACS Nano* **2017**, *11*, 4198.
[61] C. Lv, X. Yang, A. Umar, Y. Xia, Y. Jia, L. Shang, T. Zhang, D. Yang, *J. Mater. Chem. A* **2015**, *3*, 22708.
[62] P. Wan, H. Xie, N. Zhang, S. Zhu, C. Wang, Z. Yu, W. Chu, L. Song, S. Wei, *Adv. Funct. Mater.* **2020**, *30*, 2002624.
[63] M.-Q. Zhao, M. Torelli, C. E. Ren, M. Ghidiu, Z. Ling, B. Anasori, M. W. Barsoum, Y. Gogotsi, *Nano Energy* **2016**, *30*, 603.
[64] F. Zou, Y. M. Chen, K. Liu, Z. Yu, W. Liang, S. M. Bhaway, M. Gao, Y. Zhu, *ACS Nano* **2016**, *10*, 377.

Batteries & Supercaps

Research Article
doi.org/10.1002/batt.202200411

Chemistry Europe
European Chemical
Societies Publishing

[65] X. Gao, X. Dong, Z. Xing, C. Nie, G. Zheng, Z. Ju, *Adv. Mater. Technol.* **2021**, *6*, 2100207.

[66] C. Yan, X. Gu, L. Zhang, Y. Wang, L. Yan, D. Liu, L. Li, P. Dai, X. Zhao, *J. Mater. Chem. A* **2018**, *6*, 17371.

[67] X. Wu, H. Wu, B. Xie, R. Wang, J. Wang, D. Wang, Q. Shi, G. Diao, M. Chen, *ACS Nano* **2021**, *15*, 14125.

[68] C. Yan, G. Chen, X. Zhou, J. Sun, C. Lv, *Adv. Funct. Mater.* **2016**, *26*, 1428.

[69] G. Suo, J. Zhang, D. Li, Q. Yu, M. He, L. Feng, X. Hou, Y. Yang, X. Ye, L. Zhang, W. A. Wang, *J. Colloid Interface Sci.* **2020**, *566*, 427.

[70] S. Iqbal, L. Wang, Z. Kong, Y. Zhai, X. Sun, F. Wang, Z. Jing, X. He, J. Dou, L. Xu, *ACS Appl. Mater. Interfaces* **2022**, *14*, 15324.

[71] S. H. Yang, Y. J. Lee, H. Kang, S. K. Park, Y. C. Kang, *Nano-Micro Lett.* **2021**, *14*, 17.

[72] J. Chu, W. A. Wang, J. Feng, C. Y. Lao, K. Xi, L. Xing, K. Han, Q. Li, L. Song, P. Li, X. Li, Y. Bao, *ACS Nano* **2019**, *13*, 6906.

[73] X. Xu, D. Zhang, Z. Wang, S. Zuo, J. Yuan, R. Hu, J. Liu, *ACS Appl. Mater. Interfaces* **2021**, *13*, 11007.

[74] H. Wu, S. Lu, S. Xu, J. Zhao, Y. Wang, C. Huang, A. Abdelkader, W. A. Wang, K. Xi, Y. Guo, S. Ding, G. Gao, R. V. Kumar, *ACS Nano* **2021**, *15*, 2506.

[75] I. Sultana, M. M. Rahman, S. Mateti, V. G. Ahmadabadi, A. M. Glushenkov, Y. Chen, *Nanoscale* **2017**, *9*, 3646.

[76] X. Xu, F. Li, D. Zhang, Z. Liu, S. Zuo, Z. Zeng, J. Liu, *Adv. Sci.* **2022**, *9*, 2200247.